IOP Publishing Plasma Sources Science and Technology

Plasma Sources Sci. Technol. **29** (2020) 045013 (9pp) https://doi.org/10.1088/1361-6595/ab7cc0

Characterization of plasma jets driven by a small linear railgun

M K Schneider, A I Mohammed and C S Adams[1]

Virginia Polytechnic Institute and State University, Center for Space Science and Engineering Research, 1341 Research Center Drive, Suite 1000, Blacksburg VA 24061, United States of America

E-mail: csadams@vt.edu

Received 10 December 2019, revised 17 February 2020
Accepted for publication 4 March 2020
Published 3 April 2020

Abstract

This paper reports measured and inferred characteristics of plasma jets produced by a 10 cm plasma-armature railgun designed to provide a platform to study phenomena associated with high-Mach-number plasma flows. This gas-fed accelerator is powered by an underdamped LC pulse-forming network operated at charge voltages up to 15 kV and fired into a large cylindrical vacuum chamber, emitting a series of plasma jets which propagate into the chamber. Analysis of data captured by an interferometer and spectrometer at locations 10 and 40 cm away from the railgun's bore suggests jet velocities between 14.5 and 19.7 km s^{-1}, electron number densities between 3.4×10^{14} and 2.5×10^{16} cm^{-3}, a plasma temperature of approximately 2 eV, and Mach number between 5.1 and 7.0. These parameters fall in a parameter space conducive to the study of shock structures in multi-ion-species plasmas, as the ion stopping distances and consequently shock thicknesses are expected to be in the several millimeter to few-centimeter range.

Keywords: marginally-collisional plasmas, shocks, plasma jet, railgun, multi-ion plasma

1. Introduction

This paper reports results from an experimental campaign to characterize plasma jets produced by a purpose-built, gas-fed plasma-armature railgun. The investigation, conducted at the Center for Space Science and Engineering Research at Virginia Tech (Space@VT), seeks to lay the groundwork for future studies of high-Mach-number plasma jets in a parameter space such that jet stagnation produces shock structures with readily-diagnosable centimeter-scale thicknesses. This effort to understand plasma shock structures and the dynamic behavior of supersonic plasma flow is motivated in part by the need to validate physics models relevant to inertial confinement fusion (ICF). Previous work has suggested that species separation caused by shock propagation in the fusion fuel may be partially responsible for lower than expected neutron yields observed in ICF experiments [1–3]. Further motivation is found in the investigation of plasma-jet driven magneto-inertial fusion [4–6], where the formation of a cohesive, dense plasma liner from discrete plasma jets is dependent on an understanding of the dynamic behavior of merging plasma-jets in a collisional regime [7–9]. Beyond the laboratory, the role of ion-diffusion mechanisms in multi-ion-species plasma shocks is germane to the study of type-II supernovae, where computational models predict an important role of shock heating in supernovae nucleosynthesis [10, 11].

In order to effectively study the underlying multi-fluid physics, a plasma jet source was designed to operate in a regime where the thickness of shock structures formed upon jet stagnation would be on the order of centimeters. This requirement was driven by the objective of capturing space and time resolved measurements of ion species concentrations throughout the shock thickness, and imposed constraints on the ion–ion collision frequency and the jet velocity. Previous studies of jet merging suggest that such shocks are readily produced using jets with velocities of 10–20 km s^{-1}, electron number densities in the 10^{13}–10^{14} cm^{-3} range (assuming $\bar{Z}$ near unity), and ion temperatures of less than approximately 3 eV [7–9, 12].

Section 2 of this paper provides an overview of the design and operation of the plasma accelerator. Section 3 discusses the experimental apparatus and describes the diagnostics employed to characterize the plasma jets. Section 4 analyzes experimental results in order to characterize the propagation of an unobstructed single jet, establishing the parameter space of jets emitted by the railgun. Furthermore, collision parameters within

[1] Author to whom any correspondence should be addressed.

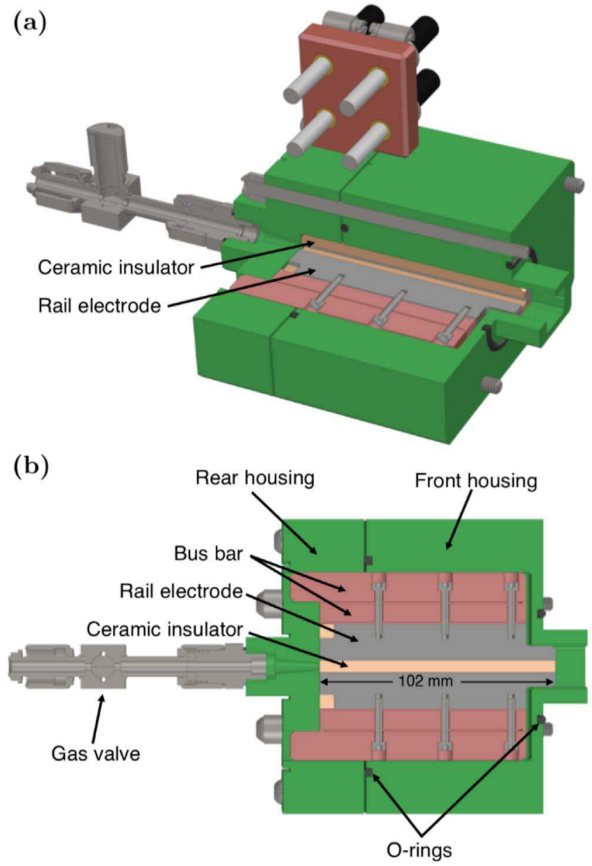

Figure 1. (a) Quarter-section view of the railgun model. (b) Top-view cross-section schematic of the accelerator showing poly-ether-ketone (PEEK) plastic body (green), chromium-copper bus bars (red), copper-tungsten alloy electrodes (white), boron-nitride and aluminum-nitride mixed ceramic insulators (gray), and gas valve. Electrode length is given for scale.

the jets are estimated in order to assess the utility of the facility to study plasma shock physics and jet interpenetration. Finally, section 5 summarizes the work presented and outlines ongoing and future studies using the accelerator.

2. Linear plasma-armature railgun

2.1. Gun design

A linear railgun configuration was chosen for the plasma-jet source for its simple geometry, suitable for a modular design. The design process was informed by the existing body of work on plasma-armatures [13, 14] and early versions of the railguns used by the Plasma Liner Experiment [6, 9, 15].

A computer rendering of the accelerator design is shown in figure 1. The design consists of 102 mm long rails and a 3.2 mm high, 5 mm wide rectangular bore. Electrodes are fastened to chromium-copper bus bars with screws and sandwiched between two identical ceramic insulators that set the electrode separation distance and bore cross-section. Bus bars are permanently mounted to the rear plastic housing. To assemble the gun, the electrodes are mounted to the bus bars and the ceramic insulators are placed above and below the electrodes before the entire assembly slides into the front housing. Two fluorocarbon O-rings fit into a groove on either end of the front housing to seal the seam between the two housing pieces as well as the seam between the gun and vacuum chamber flange to which it is mounted. Five stainless steel screws pass through both housing pieces and thread into pre-drilled and tapped holes in the vacuum chamber flange to hold the gun to the flange and maintain pressure on the O-rings. The modular internal design of the railgun eases electrode and insulator removal and replacement.

For the results presented in this paper, electrodes machined from a 55% tungsten, 45% copper alloy and insulators machined from an aluminum-nitride (AlN) and boron-nitride (BN) ceramic mixture were used for all shots. The gun is fed from a compressed gas cylinder of pure argon via a Parker Series 99 fast-actuated solenoid valve mounted to the rear of the gun. A line pressure of 700 kPa was used for all shots. A custom driver circuit delivers a slightly underdamped current waveform with half-period of $\approx$2 ms to the valve to rapidly open and close the valve poppet. Vacuum chamber rate-of-rise tests suggest that an argon mass of approximately 11 mg is puffed into the gun during each pulse. Gas flowing through the valve first travels through a converging nozzle integrated into the PEEK housing that directs gas into the bore at the breech of the gun.

2.2. Pulse-forming network (PFN)

The railgun is powered by an LC PFN containing six 1.3 μF Scyllac-style capacitors mounted in parallel along with two 100 μF capacitors in series, for a total capacitance of approximately 58 μF. Aluminum alloy bus-work was designed with inductance chosen such that the quarter period of the discharge would match the armature's time-of-flight along the rails. The PFN delivers an underdamped current waveform of $\approx$30 μs period, with peak current of 90 and 135 kA when charged to 10 and 15 kV, respectively, as characterized by an in-house fabricated Rogowski coil and shown compared to simulations of a tuned circuit model in figure 2. An R. E. Beverly III and Associates model SG-172 CM gas-filled trigatron spark gap switch controls the discharge of the current pulse through four parallel RG-213 coaxial cables to the railgun load.

3. Virginia tech experimental plasma and propulsion laboratory

Experiments are performed in a 0.76 m^3, 1.2 meter long cylindrical vacuum chamber situated adjacent to the pulse-forming network, shown in figure 3. The railgun mounts to a flange located on a hinged door at one end of the chamber with the bore-sight (or z) axis of the accelerator collinear with the axis of the chamber, as seen in figure 4. Experimental results are referenced relative to this bore-sight axis, defined as the axis aligned with the center of the railgun bore and parallel to the electrode length with $z = 0$ at the accelerator's muzzle. Eight 30 centimeter

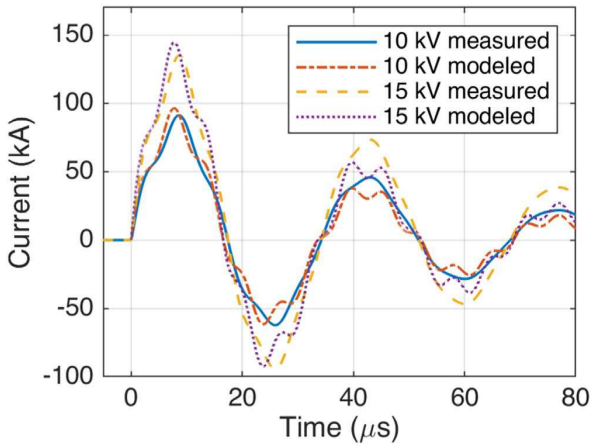

Figure 2. Comparison between observed and modeled current discharges from the pulse-forming network at charge voltages of 10 and 15 kV. The circuit model was tuned to match the period of the observed discharge by varying the inductance of the 100 μF capacitors, the only unknown parameter when the PFN was designed.

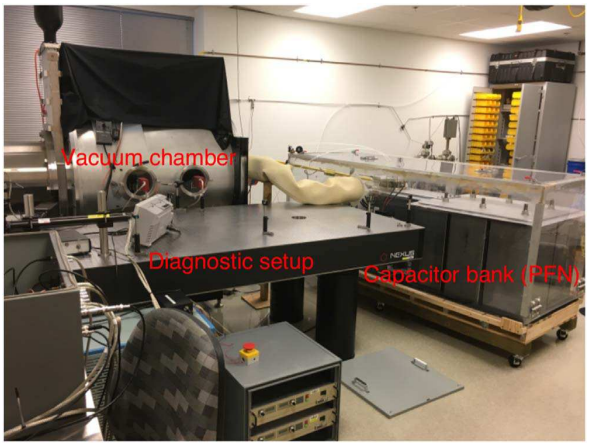

Figure 3. Laboratory apparatus including vacuum chamber, pulse-forming network, and optical table for diagnostic setup.

diameter viewports arranged in two azimuthal arrays of four ports provide diagnostic access. An oil-sealed rotary vane rough pump is first used to pump the chamber down to 50 mTorr in 60 minutes and a cryopump brings the chamber down to an ultimate pressure of ~200 nTorr.

Diagnostics mount to a 244 cm by 122 cm optical table located on one side of the chamber and a 60 cm by 30 cm optical breadboard mounted on the other. Data is acquired using a 12 bit, 8-channel National Instruments PXIe 5105 oscilloscope with 60 MHz bandwidth and 60 MSa s^{-1} sampling rate. A Stanford Instruments DG645 digital delay generator precisely times the spark gap switch, data acquisition collection, and solenoid gas puff valve for each experimental pulse. Auxiliary systems are computer-controlled via fiber-optic cable and data acquisition and control electronics are all housed in a single Faraday cage. Additionally, these acquisition and control electronics are powered by an uninterruptible

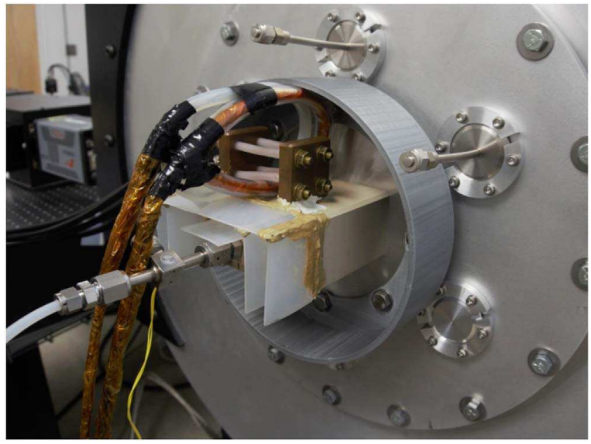

Figure 4. The railgun mounts to the vacuum chamber door with the bore of the accelerator collinear with the axis of the cylindrical chamber. Also shown is the solenoid valve that delivers gas to the breech of the gun and two Rogowski coils used to infer the magnitude of the current pulse delivered to the railgun.

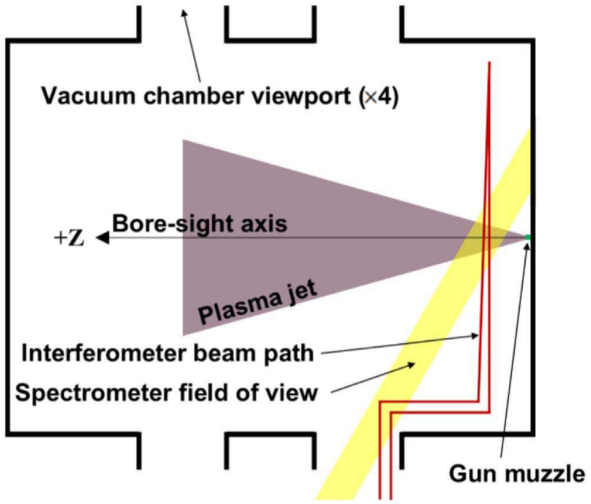

Figure 5. To-scale, top view, cross-section schematic of vacuum chamber (outlined in black) at the chamber's center axis. Diagnostic viewing chords are shown along with a representative plasma-jet trajectory.

power supply which is disconnected from utility power during each experimental pulse in order to protect equipment and prevent noise pickup by ground loops.

3.1. Diagnostics

The railgun-accelerated plasma jets are characterized by a suite of instruments consisting of a single-chord interferometer, high-resolution imaging spectrograph, compact survey spectrometer, and an image-intensified CCD camera. Figure 5 presents a top-view cross-section of the vacuum chamber detailing the diagnostic setup. All diagnostics are configured such that the field-of-view of each is in the horizontal plane and at the height of the railgun's bore; therefore,

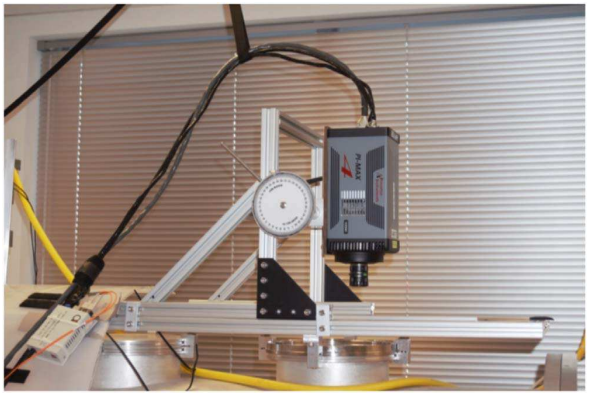

Figure 6. Image-intensified CCD camera mounted to 4 degree-of-freedom track system and positioned to photograph the plasma-jet as it emerges from the railgun's bore. Plasma-jet trajectory in the perspective of this image is from right to left.

no y-axis (height) position is given, as $y = 0$ for all diagnostics. The only exception was the image-intensified CCD camera which, as shown in figure 6, was mounted atop the vacuum chamber.

3.1.1. Single-chord interferometer. A heterodyne Mach–Zehnder interferometer is used in quadrature to infer electron number density in the plasma jets. A coherent beam from a Model 1122 P Lumentum 632 nm He–Ne laser (2 mW) with linear polarization passes through an IntraAction ATM-801A1 acousto-optic modular powered by an IntraAction ME-801 radio-frequency (RF) driver, splitting the beam and upshifting one beam by 80 MHz. The unshifted beam passes through the chamber at the location of interest before recombining with the frequency-shifted reference beam and the recombined beams illuminate a Thorlabs PDA10A photodetector with 150 MHz bandwidth. In the RF circuit, the photodetector signal is filtered by an 80 MHz centered bandpass filter (MCV Microwave BCL80-40-A1) to remove any components other than the carrier beat frequency before being mixed with the reference RF signal by a Pulsar IDO-04-412 IQ demodulator. Finally, the I and Q mixer outputs are filtered through two 6 MHz lowpass filters to remove the 80 MHz carrier frequency from the quadrature signals before digitization. For the results presented in this paper, the probe beam was in a double-pass configuration, intersecting the bore-sight axis at one of three distances from the gun muzzle: $z = 10.2$, 20.3, or 40.6 cm.

In our analysis, we assume the mean charge state $\bar{Z}$ is approximately unity and consequently that measured phase shift is dominated by the presence of free electrons and that the phase shift contributions from ions and neutrals are negligible. With these assumptions the phase shift is proportional to chord-integrated electron number density, and for a laser wavelength of 632.8 nm is given by (in cgs units)

$$\Delta\phi = 1.778 \times 10^{-17} \int n_e \mathrm{d}\ell \ , \tag{1}$$

where n_e is the electron number density, ℓ is the path length of the probe beam through the plasma, and phase shift ϕ is found from the arctangent of the ratio of the two digitized signals, $S(t)_Q$ and $S(t)_I$, which respectively represent the sine and cosine of the phase shift.

3.1.2. Fast photography. Photographs of plasma jets are captured with a Princeton Instruments PI-MAX4 1024i image-intensified 1024 × 1024 pixel camera capable of gate times as short as 3 ns, equipped with a broad-spectrum photocathode (200–900 nm). The lens used with the camera is a 25 mm fixed focal length lens with f/8 aperture. The camera was mounted atop the vacuum chamber, capturing top-down images normal to the direction of jet propagation, as seen in figure 6.

3.1.3. Spectroscopy. Radiation emitted by the plasma is collected and analyzed using a Princeton Instruments Acton Series SP-2758 750 mm high-resolution imaging spectrograph with interchangeable gratings (300, 2400, and 3600 g mm^{-1}) equipped with the same iCCD imaging unit discussed in section 3.1.2. An optical system employing a 7.6 cm objective lens collects and focuses light originating within a 7.6 cm diameter column in front of the lens onto a multi-mode fiber-optic cable coupled to the spectrograph's entrance slit. As a result, spectral data collected for the experiments presented in this paper are spatially averaged and are also temporally integrated over the shot length (∼200 μs) due to the long exposure times necessitated by low emission intensity. Similar to the interferometer probe beam, the spectrograph's optics were configured such that the center of the viewing region intersected the bore-sight axis of the accelerator at the same three distances from the gun muzzle as for the interferometer: $z = 10.2$, 20.3, and 40.6 cm. The angle between the axis of the viewing region and the bore-sight axis varied from ≈50° for measurements at $z = 10.2$ cm to ≈80° for measurements at $z = 40.6$ cm. The 300 g mm^{-1} grating was used for all the data presented (providing 18 pixel nm^{-1} dispersion when used with the PI-MAX4 CCD) and the spectrograph's entrance slit width was set to between 10 and 50 μm depending on the bore-sight axis intersection distance, resulting in a minimum spectral line-width resolution between 0.157 and 0.217 nm, respectively.

In addition to the high-resolution spectrograph, a compact spectrometer (Thorlabs CCS100) is used to collect spectral data in the visible range with a 10 pixel nm^{-1} dispersion. This spectrometer surveys spectral lines with a wavelength between 350 and 700 nm, time-integrated during each shot. Although the wavelength resolution is low compared to the Princeton Instruments spectrograph, data from this instrument allow us to identify which ion species are contributing to line emission in the spectra and provide insight regarding the composition of the jets.

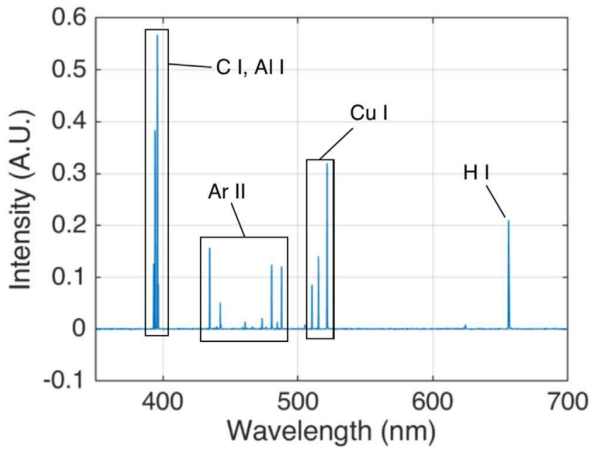

Figure 7. Typical visible-range, time-integrated spectral data taken at $z = 10.2$ cm used to analyze jet composition. Singly-ionized argon spectral lines fall between 440 and 500 nm.

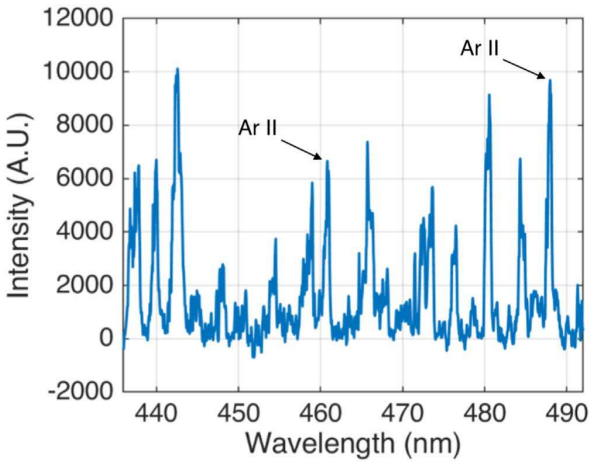

Figure 8. Spectrogram for shot 408 with the two singly-ionized argon lines used for temperature estimation indicated, $z = 10$ cm and $V_{PFN} = 15$ kV for this shot.

4. Measurements of jet properties

The following results characterize plasma jets formed while supplying the railgun with pure argon. Prior to each shot the manifold supplying the railgun was pressurized to 700 kPa and during each shot sequence approximately 11 mg of argon was injected by the fast pulse valve. For roughly half of the 71 shots in this campaign (shots 395–465), the PFN was charged to 10 kV and for the remaining shots, to 15 kV.

4.1. Jet composition

In addition to ionized and neutral argon, the plasma jets also contain impurity species that are ablated from the internal railgun structure and accelerated along with the argon. In order to estimate the mass fraction of argon in the jets as they leave the accelerator, the change in pressure inside the vacuum chamber following each shot is recorded. By comparing this pressure to the pressure rise recorded when argon was puffed into the chamber without discharging the capacitor bank, the average percent concentration of argon in the jets by mass is 48.0 ± 4.3%. This average is for both the 10 and 15 kV capacitor bank charge voltages, as there was no statistical difference between the two cases.

Figure 7 shows a typical spectrum captured by the compact spectrometer. Singly-ionized argon lines are recorded with wavelengths between 440 and 500 nm, as outlined in the figure. By comparing the wavelengths of the remaining lines to the data tabulated in the NIST Atomic Spectra Database [16], the most prominent impurity line emission is attributable to a mixture of hydrogen, carbon, and copper.

4.2. Temperature

Plasma jet temperature was estimated from the ratio of observed intensities of spectral lines. Assuming local thermodynamic equilibrium (LTE) and an optically thin plasma, this method relates the temperature to the ratio of intensities between two spectral lines from the same species and ionization state by [17]

$$\frac{I_1}{I_2} = \frac{g_1}{g_2}\frac{A_1}{A_2}\frac{\lambda_2}{\lambda_1} e^{\left[-\left(\frac{E_1-E_2}{kT}\right)\right]}, \tag{2}$$

where I is intensity, g is the statistical weight of the transition's higher energy level, A is the transition probability, λ is the wavelength, E is the higher energy level of the transition, and T is the plasma temperature.

Figure 8 shows a typical spectrogram and identifies two singly-ionized argon lines used to estimate temperature, at $\lambda = 460.96$ nm and $\lambda = 487.99$ nm. Although many other Ar II lines were present in each shot, these two were chosen for the large difference between the upper energy level, E, of each transition. Choosing line pairs with $E_1 - E_2$ as large as practical reduces the sensitivity of the temperature estimate to error in measured intensity. The value of E and the other spectral transition constants were acquired from the NIST Atomic Spectra Database [16].

As is the case with jets produced by other plasma accelerators operating in a similar regime [6], it is unlikely that these jets are in LTE during the entirety of jet propagation [18]; therefore, a detailed comparison of temperatures across different gun parameters would be premature. Instead, the temperature analysis here provides a rough estimates with which plasma jet collision parameters and penetration lengths relevant to future work can be estimated. To this end, the average plasma temperature estimated via the ratio method across all gun parameters and diagnostic settings is $T = 2.0 \pm 0.9$ eV. Future studies will employ detailed atomic transition modeling to predict non-LTE spectral emission and more accurately estimate plasma jet temperature.

4.3. Density and jet profile

Plasma density was inferred from line-integrated electron-number-density measurements and jet widths estimated from visible spectrum fast camera images. In order to qualitatively

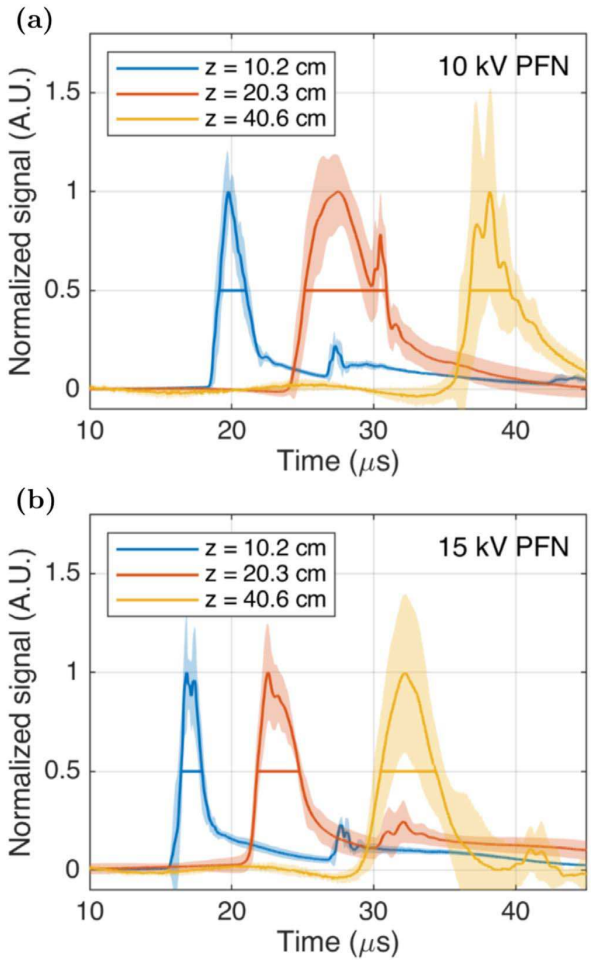

Figure 9. (a) Normalized and averaged interferometer phase shift signals versus time with plus or minus one standard deviation for shots taken with 10 kV PFN charge voltage. FWHM of the average signal is also shown and was used to calculate average jet thickness. (b) The same data for the 15 kV PFN charge voltage case.

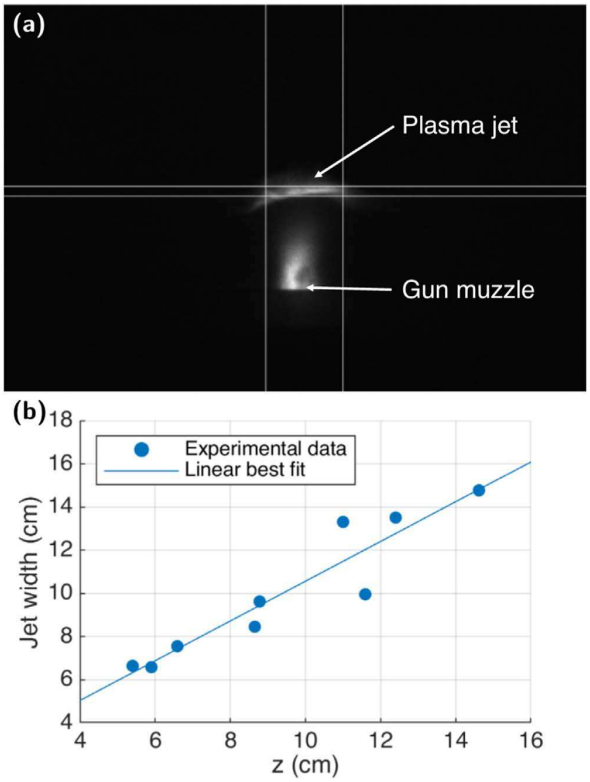

Figure 10. (a) Visible spectrum, gray-scale, image-intensified photograph captured with a 3 ns gate width, f/8 aperture, at $t = 15$ μs. The camera line of sight is normal to jet velocity such that the jet is traveling upward. Vertical white bars denote the jet width inferred for this shot. (b) Scatter plot of jet widths estimated from iCCD images as a function of jet leading edge z-axis position and a best linear fit overlaid.

represent the translation of the jets, figure 9 shows the evolution of mean phase shift from 5–10 shots per average trace normalized to peak mean phase shift at each distance from gun muzzle for both PFN charge voltages. The rapid rise and fall of the phase shift in these traces is interpreted to mean that a plasma jet has been emitted and is propagating through the chamber as a cohesive mass with distinct leading and trailing edges. Figure 10 shows a representative visible–near-infrared spectrum photograph (taken with a 3 ns gate width, 15 μs after the gun was fired) capturing a plasma jet translating through the chamber (velocity vector is upwards in the figure). The sudden change in intensity from the image background to plasma jet at the leading edge of the jet supports this qualitative interpretation of figure 9.

Also evident in figure 9 is the emission of multiple jets during the course of each experimental pulse. For both the 10 and 15 kV PFN charge voltages, a second jet passes the chord at 10.2 cm near $t = 27$ μs. The magnitude of the phase shift recorded by the interferometer during the passage of this second jet is much less than that for the first jet, which is interpreted as an indication that the density of the second jet is significantly lower than that of the first jet. Furthermore, the second jet appears to move at a significantly higher velocity than the first jet, arriving at the chord positioned at 20.3 cm near $t = 32$ μs and at the 40.6 cm chord near $t = 42$ μs for the 15 kV case.

Short-gate-time images of the plasma were used to estimate jet width (of the first jet) as a function of z-axis position of the jet's leading edge. Calibration images of the optical breadboard mounted inside the chamber with a square grid of mounting holes were used to map positions on the breadboard to positions in the horizontal plane at the bore-sight axis of the gun, and finally to pixel locations at the image plane. Then, fast camera images such as figure 10 were used to infer the lengths of and distances between features based on pixel coordinates in each image along that plane. The jet width for a given image was estimated by binning intensities in all columns within the set of rows representing jet z-axis thickness (denoted by the horizontal white lines in figure 10(a)) and then taking the full-width, half-maximum (FWHM) of that binned line-out as the jet width (denoted by the vertical white

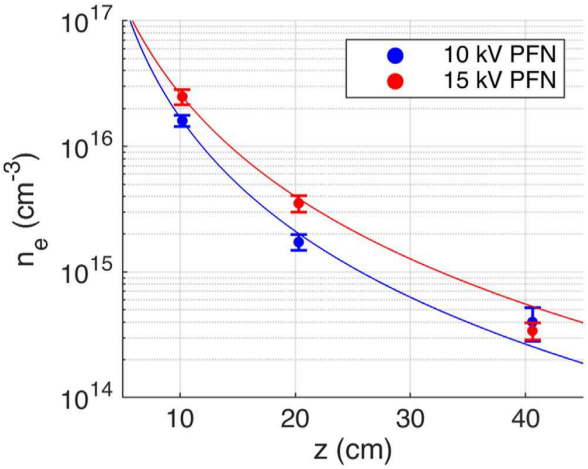

Figure 11. Average electron number density of the first jet emitted with one standard deviation error bars comparing PFN charge voltage and interferometer chord position z. The line superimposed onto the plot shows a semi-analytical prediction of jet density assuming adiabatic expansion and using the 10.2 cm experimental measurement as a reference point.

lines in figure 10(a)). By conducting the same analysis for images taken at different times after the PFN is triggered, we determined that the width of the first jet can be approximated as a function of distance from the gun muzzle by $w = 0.92z + 1.37$ where z is the distance along the bore-sight axis to the leading edge of the jet and w is the width of the jet at the leading edge location in centimeters. By replacing $d\ell$ in equation (1) with this expression for w and accounting for the fact that the interferometer is in a double-pass configuration, electron number density per cubic centimeter is estimated by

$$n_e = \frac{\Delta\phi}{3.27 \times 10^{-17} z - 4.87 \times 10^{-17}}. \quad (3)$$

Figure 11 compares the peak electron number density for both the 10 and 15 kV PFN charge voltage cases at each position along the bore-sight axis, as discussed in section 3.1.1. For the 10 kV case, the average peak jet density decreases from 1.6×10^{16} to 1.7×10^{15} to 4.0×10^{14} cm^{-3} from $z = 10.2$ to 20.3 to 40.6 cm, respectively. For the 15 kV case, the average peak jet density decreases from 2.5×10^{16} to 3.5×10^{15} to 3.4×10^{14} cm^{-3} from $z = 10.2$ to 20.3 to 40.6 cm, respectively. Jets are accelerated into the chamber with very low base pressure (<1 μTorr) where we expect a negligible collision rate between the jets and background molecules in the chamber; therefore, the reduction in jet density as a function of z-axis position should correlate roughly with adiabatic expansion of the gas. Figure 11 also displays traces of a semi-analytical prediction of jet density assuming expansion under these conditions that approximately matches the changes in density inferred from chord-integrated measurements. For this model, a cylinder with center axis aligned with the gun's bore-sight axis is used to represent the plasma volume, which contains constant mass. Changes in volume are calculated as a function of z-axis position where diameter is equal to jet width as discussed previously and cylinder length is based on expansion at the plasma's ion thermal speed. The $z = 10.2$ cm data point for each PFN charge voltage is used as the reference density of adiabatic expansion of the jet.

Table 1. Comparison of the times of peak interferometer phase shift for changing PFN charge voltage and interferometer probe beam position. Estimated average velocity of the first jet for each PFN charge voltage is based on the average time of peak phase shift at each position.

V_{PFN} (kV)	z (cm)	$t_{\phi_{max}}$ (μs)	u_{jet} (km s^{-1})	$\mathcal{M}_{estimate}$ ($T = 2.0$ eV)
10	10.2	22.1 ± 0.60		
10	20.3	29.8 ± 1.50	14.5 ± 3.9	5.1 ± 1.4
10	40.6	44.4 ± 4.02		
15	10.2	18.3 ± 0.27		
15	20.3	24.0 ± 0.60	19.7 ± 2.6	7.0 ± 0.9
15	40.6	34.1 ± 1.38		

In order to approximate jet thickness (z-axis length), the FWHM of the interferometer phase-shift signal spike in each shot was measured and averaged. In order to visualize this process, the FWHM of each average interferometer phase-shift trace is also plotted in figure 9. The average velocity for each PFN charge voltage case shown in table 1 was used along with the average FWHM time calculated from the phase-shift traces to predict average jet thicknesses. For the 10 kV PFN charge voltage case, jet thickness was estimated as 2.4, 7.2, and 3.4 cm, and for the 15 kV case jet thickness was estimated as 2.6, 5.6, 7.6 cm for the $z = 10.2$, 20.3, and 40.6 cm locations, respectively. It should be noted that the significant thickness of the jet estimated at 20.3 cm for the 10 kV case was likely influenced by the second jet catching up with the first jet shortly after $t = 30$ μs.

4.4. Velocity and Mach number

The bulk velocity of the plasma jets is estimated from the time-of-flight of the peak interferometer phase shift between the three interferometer chord positions (10.2, 20.3, and 40.6 cm) for 10 and 15 kV PFN charge voltages. Since the single-chord interferometer collected data at only one position along the z-axis during each shot, an average jet velocity was estimated using data from multiple shots with the same operating parameters. Specifically, to robustly estimate the average time-of-flight between chord positions, the velocity of the first jet was inferred for every combination of chord positions for each PFN voltage within this group of 71 shots. The mean and standard deviation of these binary-shot velocity inferences was then calculated for each of the two PFN charge voltage cases, resulting in the estimates shown in table 1. Using these estimates of velocity of the first jet, assuming a plasma temperature of 2.0 eV (see section 4.2), and pure Argon jet composition, the Mach number, $\mathcal{M}$ was estimated and is also shown in table 1. The Mach number of the jets is

defined as [19, 20]

$$\mathcal{M} = \frac{u_{\text{jet}}}{\sqrt{\gamma \bar{Z} \frac{k_B T_e}{\bar{m}_i}}}, \tag{4}$$

where γ is the adiabatic index, $\bar{Z}$ is the mean charge state, $\bar{m}_i$ is the average ion mass, T_e is the electron temperature, k_B is the Boltzmann constant, and u_{jet} is the bulk plasma jet velocity.

Note that the velocity and Mach number estimates in table 1 pertain only to the first jets emitted by the railgun. Similar time-of-flight estimates of the less massive second jet suggest velocities of at least 20 km s^{-1} for both the 10 and 15 kV cases. However detailed analysis of the characteristics of this later jet are left to future work.

4.5. Collision parameters relevant to future study of colliding jets

Using the estimate of plasma temperature above as well as the jet velocity and density data presented in previous sections, we can estimate plasma collision parameters such as ion–ion collision rate and ion penetration distance to aid in understanding collisionality as it pertains to plasma shocks and interactions between plasma jets. As with other plasma jets in a similar parameter space [7], we estimate the ion–ion collision rate for counter-streaming ions to be the limiting factor for jet interpenetration. This collision rate, $\nu_s^{i|i'}$, is approximated in the fast-ion limit as [20]

$$\frac{\nu_s^{i|i'}}{n_{i'} Z^2 Z'^2 \lambda_{ii'}} \approx 9.0 \times 10^{-8} \left(\frac{1}{\mu} + \frac{1}{\mu'} \right) \frac{\mu^{1/2}}{\epsilon^{3/2}}, \tag{5}$$

where the Coulomb logarithm, $\lambda_{ii'}$ is given by

$$\lambda_{ii'} = 43 - \ln \left[\frac{ZZ'(\mu + \mu')}{\mu \mu' \beta_D^2} \left(\frac{n_e}{T_e} \right)^{1/2} \right] \tag{6}$$

and the field particle parameters are represented by a prime, Z is the mean charge state, μ is the average ion to proton mass ratio, ϵ is the test particle kinetic energy, β_D is fractional velocity compared to the speed of light defined as $\beta_D = v_D/c$, c is the speed of light, n_i and n_e are the ion and electron densities, respectively, and T_e is the electron temperature. Units are cgs and ϵ and T_e are in eV. Mean charge state is assumed to be 1 for this estimation and although it was estimated in section 4.1 that jets are about 50% argon, these estimates assume 100% argon jets. While this simplification may slightly alter the result, since the impurity species identified using spectral data consist of both high and low Z ions as compared with argon, the average ion mass of the jets is roughly the same as for pure argon jets. The hypothetical jet collision geometry considered is a jet exiting the railgun's bore and colliding with a stagnant plasma of equal temperature and density (see section 5); therefore, ϵ is calculated using the velocity calculated in section 4.4 and the test and field particle parameters are all equal. Finally, the ion penetration distance in this scenario is given by [7]

$$\lambda_i^s \approx \frac{u_{\text{jet}}}{4\nu_s^{i|i'}}. \tag{7}$$

Table 2. Comparison of counter-streaming ion collision rate and ion penetration length for changing PFN charge voltage and jet translation distance.

V_{PFN} (kV)	z (cm)	$\nu_s^{i\|i'}$ (s^{-1})	λ_i^s (cm)
10	10.2	1.2×10^7	0.030
10	20.3	1.5×10^6	0.24
10	40.6	3.8×10^5	0.96
15	10.2	8.0×10^6	0.062
15	20.3	1.3×10^6	0.39
15	40.6	1.4×10^5	3.6

Table 3. Range of repeatably-achievable plasma jet parameters observed for the operating parameters presented.

Jet parameter space	
n_e (cm^{-3})	3.4×10^{14}–2.5×10^{16}
u_{jet} (km s^{-1})	14.5–19.7
T_e (eV)	≈2
$\mathcal{M}$	5.1–7.0
$\nu_s^{i\|i'}$ (s^{-1})	1.4×10^5–1.2×10^7
λ_i^s (cm)	0.030–3.6

Table 2 gives collision rates and ion penetration lengths calculated based on estimations of density at each location, average velocity for the two PFN charge voltages, and average electron temperature for the entire data set. The ion penetration distance is a strong function of distance from the gun muzzle, varying by over two orders of magnitude over the 30 cm range explored in this research.

5. Summary and future research

The experimental campaign reported here sought to characterize the parameter space accessible in an experiment where centimeter-scale supersonic plasma jets are accelerated into a large vacuum chamber by a parallel-plate railgun. The purpose of this experiment is to develop a platform to study the behavior of multi-ion-species plasma jets in a marginally-collisional regime such that any shock structures are readily diagnosable. To that end, the range of ion penetration distances inferred from diagnostic measurements appears to remain in a collisional to marginally-collisional regime, as λ_i^s grows by orders of magnitude but remains less than the thickness of the jet as the jet travels 30 cm through the vacuum chamber. Should the observed jets stagnate or collide with stagnated plasma of similar density and composition, we would expect shocks to form with thickness comparable to λ_i^s. Analysis of spectrograms of visible-ultraviolet radiation emitted by the translating jets indicates that the jets contain argon ions and numerous impurity ions ranging from hydrogen to copper. Table 3 shows the envelope of plasma jet

parameters that we infer to be accessible in collisions involving the first jet emitted by the railgun.

This parameter space lends itself to measurement of ion species distributions across the thickness of ion shocks induced in these jets. The thickness of shocks within these jets can be controlled over a readily diagnosible range, up to several centimeters by inducing collisions at differing distances from the muzzle of the railgun. Ongoing experimental campaigns are gathering spatially-resolved spectrograms in the vicinity of shocks, which will be reported on in future publications.

Acknowledgments

The authors are grateful for the efforts of numerous student researchers over the years for their technical support in building and operating this apparatus and associated diagnostics, with special mention to Marius Popescu, Michael Sherburne, and Matthew Carrier. This work was supported in part by the National Science Foundation under Grant No. PHY-1903442.

ORCID iDs

C S Adams https://orcid.org/0000-0003-3205-8082

References

[1] Amendt P, Wilks S C, Bellei C, Li C K and Petrasso R D 2011 *Phys. Plasmas* **18** 056308
[2] Bellei C, Amendt P A, Wilks S C, Haines M G, Casey D T, Li C K, Petrasso R and Welch D R 2013 *Phys. Plasmas* **20** 012701
[3] Kagan G and Tang X Z 2014 *Phys. Lett.* A **378** 1531–5
[4] Parks P B 2008 *Phys. Plasmas* **15** 062506
[5] Langendorf S J and Hsu S C 2017 *Phys. Plasmas* **24** 032704
[6] Hsu S C *et al* 2012 *Phys. Plasmas* **19** 123514
[7] Merritt E C, Moser A L, Hsu S C, Adams C S, Dunn J P, Miguel Holgado A and Gilmore M A 2014 *Phys. Plasmas* **21** 055703
[8] Merritt E C, Moser A L, Hsu S C, Loverich J and Gilmore M 2013 *Phys. Rev. Lett.* **111** 085003
[9] Hsu S C *et al* 2015 *J. Plasma Phys.* **81** 345810201
[10] Woosley S E, Arnett W D and Clayton D D 1973 *Astrophys. J. Suppl. Ser.* **26** 231
[11] Woosley S E and Weaver T A 1995 *Astrophys. J. Suppl. Ser.* **101** 181
[12] Moser A L and Hsu S C 2015 *Phys. Plasmas* **22** 055707
[13] Parker J V 1989 *IEEE Trans. Magn.* **25** 418–24
[14] Batteh J H 1991 *IEEE Trans. Magn.* **27** 224–7
[15] Witherspoon F D, Case A, Messer S J, Bomgardner R, Phillips M W, Brockington S and Elton R 2009 *Rev. Sci. Instrum.* **80** 083506
[16] Kramida A, Ralchenko Y, Reader J and NIST ASD Team 2018 NIST Atomic Spectra Database (ver. 5.6.1). National Institute of Standards and Technology, Gaithersburg, MD (https://doi.org/10.18434/T4W30F)
[17] Griem H R 1964 *Plasma Spectroscopy* (New York: McGraw-Hill) (https://doi.org/10.1126/science.147.3655.284)
[18] Hutchinson I H 2002 *Principles of Plasma Diagnostics* 2nd edn (Cambridge: Cambridge University Press) (https://doi.org/10.1017/CBO9780511613630)
[19] Chen F F 1984 *Introduction to Plasma Physics and Controlled Fusion* 2nd edn (New York: Plenum Press) (https://doi.org/10.1007/978-3-319-22309-4)
[20] Huba J D *et al* 2013 *NRL Plasma Formulary* (Washington, DC: Naval Research Laboratory)